Check for updates

Highly active conversion of CO_2 to CO on AuCuB materials†

Yuting Liu,‡[a] Yuan Fang, [iD] ‡[a,b] Qinghong Yuan, [iD] *[b] Jiaxing Lu [iD] [a,c] and Huan Wang [iD] *[a,c]

The electrochemical CO_2 reduction reaction is an attractive solution for converting CO_2 into reusable chemicals. However, the low activity of the catalysts restricts its widespread application for conversion. This study uses a simple one-pot method to prepare B-doped AuCu alloy (AuCuB) materials. AuCuB-400 demonstrated a superior faradaic efficiency (FE) for CO [99% at −1.16 V *vs.* the reversible hydrogen electrode (RHE)], whereas the FE_{CO} of AuCu was much lower (42%). Operando electrochemical Raman spectroscopy and density functional theory (DFT) calculations revealed that incorporating B could tune the electronic structure of AuCu to promote the adsorption of CO intermediates, thus facilitating the conversion of CO_2 to CO. These findings will provide a good approach for designing highly active alloy catalysts for converting CO_2 to CO.

Increasing CO_2 emissions have resulted in various issues, such as global warming and rising sea levels.[1] Various approaches have been proposed to capture and utilize CO_2 to mitigate these serious issues.[2,3] One of the most promising approaches is the electrochemical CO_2 reduction reaction (CO_2RR), which represents a straightforward and environment-friendly strategy to transform CO_2 into valuable products (CO, HCOOH, C_2H_4, *etc.*).[4–6] However, some intrinsic challenges dramatically hinder the development of this method, such as poor selectivity, low partial current density, and low faradaic efficiency (FE).[7] Numerous efforts have been devoted to this field to solve these problems, including designing electrocatalysts and optimizing electrolytes, electrolyzers, and ion exchange membranes.[8–12]

Exploring efficient and robust electrocatalysts are an important part of CO_2RR,[13] because they can reduce the energy barrier of the reaction and improve the selectivity of specific products. Although some non-metal materials exhibit superior FE_{CO},[14–16] metal catalysts have better conductivity and higher current density than non-metal catalysts. Among various metal catalysts, Au is a well-known electrocatalyst for CO_2RR to form CO. However, its high cost limits its commercial development and application.[17,18] Therefore, Au-transition bimetallic materials have been reported to reduce the cost while improving the catalytic efficiency.[19] For example, the maximum FE_{CO} of the ordered Au–Cu catalyst synthesized by the Yang group is 80%, which is significantly greater than those of pure Au-catalysts reported previously.[20] Additionally, the performance of the catalysts can be further improved by the incorporation of non-metallic atoms, such as nitrogen,[21] boron (B),[22–28] and sulfur.[29] This is because of the adjustment of valence electrons or structure of the catalyst. B is quite favored among these non-metallic atoms because of its high electronegativity, which helps with electron transfer to alter the energetics of the reaction intermediates by shifting the d-band center or electrostatic interactions and promotes electrocatalytic performance.[27,30–32] Catalysts doped with B, such as B-doped Ag nanosponges,[33] B–Pd interstitial nanocrystals,[34] and PdRuBP nanospine assemblies,[35] have been widely used in electrochemistry, exhibiting excellent catalytic activity. The study of B-doped Pd catalysts revealed higher formate production over a wide potential range compared to undoped Pd. The result can be attributed to the downshift of the d band center of surface Pd atoms due to the charge transfer between B and Pd after doping B.[36] Han *et al.* revealed that under the impact of charge transfer between Cu and B, a B-doped oxide-derived-Cu catalyst exhibited higher FE_{C_2} products (C_2H_4, C_2H_6 and C_2H_5OH, 48.2%) than a B-free oxide-derived-Cu catalyst (30.5%).[37] Although B-modified metallic materials have been studied in several literature reports, achieving a higher FE

[a]Shanghai Key Laboratory of Green Chemistry and Chemical Process, School of Chemistry and Molecular Engineering, East China Normal University, 3663 North Zhongshan Rd., Shanghai 200062, China. E-mail: hwang@chem.ecnu.edu.cn
[b]State Key Laboratory of Precision Spectroscopy, School of Physics and Electronic Science, East China Normal University, 500 Dongchuan Road, Shanghai 200241, China. E-mail: qhyuan@phy.ecnu.edu.cn
[c]Institute of Eco-Chongming, 20 Cuiniao Road, Chenjia Town, Chongming District, Shanghai 202162, China
†Electronic supplementary information (ESI) available. See DOI: https://doi.org/10.1039/d2gc04659h
‡These authors contributed equally to this work.

toward a specific product remains a significant challenge in CO_2RR.

Herein, this study presents a B-doped AuCu alloy (AuCuB) for efficient CO_2RR. Operando electrochemical Raman spectroscopy and density functional theory (DFT) calculations were combined to obtain convincing evidence that AuCuB shows significant activity in converting CO_2 to CO, owing to improved *COOH adsorption.

The AuCuB-400 material was synthesized by reducing $HAuCl_4·H_2O$ and $CuCl_2·2H_2O$ in an N,N-dimethylformamide (DMF) solution using $NaBH_4$ as a boron source and reducing agent. For comparison, the same procedure was used to synthesize the AuCu-400 material; however, DMF was replaced by H_2O (refer to the ESI† for details). The results of inductively coupled plasma-atomic emission spectrometry (ICP-AES) indicated that ca. 3.93 at% of B was doped in AuCuB-400 catalysts, but no B was detected in AuCu-400. X-ray diffraction (XRD) was conducted to confirm the crystal structure of AuCu-400 and AuCuB-400. As shown in Fig. 1A, the five diffraction peaks at 2-theta values of 38.1°, 44.3°, 64.5°, 77.6°, and 81.7° corresponded to the crystal planes of (111), (200), (220), (311), and (222) for the AuCu-400 material, respectively. The diffraction peaks of the AuCuB-400 material shifted to higher angles. For both AuCuB-400 and AuCu-400, the absence of distinct Cu diffraction peaks and the similar molar ratio of Cu and Au (1 : 2.8, by ICP-AES) indicate that Cu and Au exist in the form of an alloy. Notably, when compared with AuCu-400, the main shift in the diffraction peak of AuCuB-400 implies that B doping caused the lattice expansion, which is consistent with the previously reported literature.[36]

Transmission electron microscopy (TEM) images (Fig. 1B and C) showed that the as-synthesized AuCu-400 and AuCuB-400 were mainly composed of nanoparticles. The corresponding particle size distribution histograms of AuCu-400 and AuCuB-400 were comparable (5.5–6 and 4.5–5.5 nm, Fig. S1†). The lattice fringes with d-spacings of 0.224 and 0.234 nm corresponded to the (111) planes of AuCu-400 and AuCuB-400 (Fig. 1D and E), respectively, which were analyzed
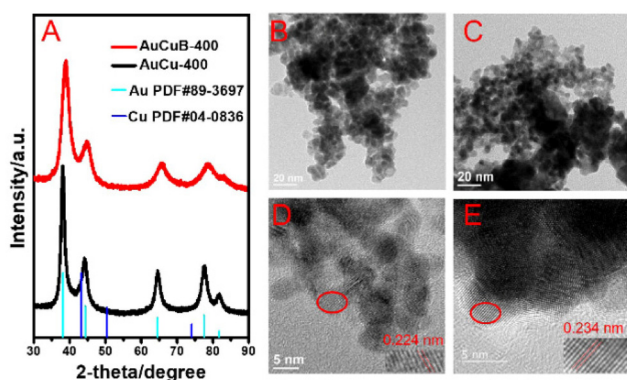
by high-resolution transmission electron microscopy (HRTEM). Compared with AuCu-400, the interplanar spacing of AuCuB-400 was enlarged due to the effective B-doping. Combining the results of XRD, HRTEM and ICP-AES, it can be observed that B was successfully incorporated into the crystal lattice of AuCu-400.

To understand the preparation process, some controlled experiments have been carried out (Table S1†). Interestingly, no B was detected in Au(B) when $CuCl_2·2H_2O$ was not added to the reaction solution (entry 2), whereas no solid material was obtained in the absence of $HAuCl_4·H_2O$ (entry 3), indicating that Cu was not reduced in this case. These suggest that the coexistence of three substances in DMF (entry 1) is key to the synthesis of AuCuB. The possible reactions of $NaBH_4$ are shown in Fig. S2.† The decomposition of BH_4^- in DMF may occur on the surface of AuCu (or Cu) (entries 1, 4 and 6), which contributes to the doping of B.

To investigate the electrocatalytic performance of the two materials for CO_2RR, linear sweep voltammetry (LSV) measurements were conducted. As shown in Fig. 2A, the hydrogen evolution reaction occurred inevitably under an N_2 atmosphere (black curve). Under CO_2-saturated conditions, an obvious increase in the current density of AuCuB-400 was detected, which can be attributed to the electroreduction of CO_2 (red curve). Additionally, a positive shift in the onset potential

Fig. 2 (A) LSV curves recorded at a scan rate of 50 mV s⁻¹ in 1 M KOH for AuCuB-400. (B) LSV curves recorded at a scan rate of 50 mV s⁻¹ for AuCu-400 (black line) and AuCuB-400 (red line) in 1 M KOH under a CO_2 atmosphere. (C) FE and J_{CO} measured at various potentials for the AuCu-400 and AuCuB-400 catalysts. (D) FE_{CO} and J_{CO} on AuCu-400, AuCuB-300, AuCuB-400, and AuCuB-500 at −1.16 V vs. RHE. (E) Long-term electrolysis of AuCuB-400 at −1.16 V vs. RHE.

Fig. 1 X-ray diffraction (A) of AuCu-400 (black line) and AuCuB-400 (red line). TEM images (B and C) and the corresponding HRTEM images (D and E) of AuCuB-400 (B and E) and AuCu-400 (C and D).

occurred from the initial −0.40 to −0.10 V. Similar behaviors were observed for AuCu-400 (Fig. S3†). A controlled experiment was conducted between AuCuB-400 and AuCu-400 to examine the effect of B incorporation in CO_2RR. As shown in Fig. 2B, the onset potential of AuCuB-400 (−0.10 V *vs.* RHE) was more positive than that of AuCu-400 (−0.25 V *vs.* RHE), indicating the excellent CO_2RR performance of AuCuB-400 as the catalyst.

To further investigate the catalytic activity and selectivity of the AuCu-400 and AuCuB-400 materials in CO_2RR, potentiostatic electrolysis was conducted in CO_2-saturated 1 M KOH solution with a gas diffusion electrode. As shown in Fig. 2C, in the case of the AuCuB-400 material, the major products were CO and H_2, while the constituents of products using AuCu-400 were significantly complex (CO, HCOOH, H_2, C_2H_4, and C_2H_5OH), revealing the high selectivity of AuCuB-400 in CO_2RR for CO. Additionally, from −0.96 to −1.36 V *vs.* RHE, the AuCuB-400 catalyst displayed much higher FE_{CO} and J_{CO} values than AuCu-400, indicating the advantage of AuCuB-400 in CO_2RR to form CO, which can be distinctly attributed to the incorporation of B. The application of AuCuB-400 even achieved a remarkable FE_{CO} of 99% when the testing potential was −1.16 V *vs.* RHE, indicating the high activity of AuCuB-400 in CO_2RR to form CO. These values are higher than those of most of the existing high performance materials for converting CO_2 to CO (Table S2†).

The effect of the B content on the catalyst activity was further investigated. In this case, AuCuB-300 and AuCuB-500 were synthesized by altering the amount of $NaBH_4$ to 300 and 500 µmol (Table S3 and Fig. S4, S5†). Overall, AuCuB-400 outperformed the other AuCuB materials in terms of catalytic performance (Fig. S6†). When the potential was set at −1.16 V *vs.* RHE, the maximum FE_{CO} for AuCuB-300, AuCuB-400, and AuCuB-500 was 65%, 99%, and 88%, respectively (Fig. 2D), demonstrating a trend of decline after increasing with an increase in the B content. The partial current density for CO showed a similar trend with the increase in the B content (Fig. 2D).

The stability in catalytic activity is essential for electrocatalysts. Hence, the long-term electrolysis of AuCuB-400 was conducted using chronoamperometry (Fig. 2E). Negligible decay was observed in both current density and FE_{CO} during the continuous electrolysis (approximately 6.5 h). Moreover, no obvious morphological changes and B leaching (from 3.93 at% to 3.50 at%) of AuCuB-400 were observed after long-term electrolysis by TEM and ICP-AES (Fig. S7†), implying its high stability.

Electrochemical impedance spectroscopy was performed to further investigate the reaction kinetics of the AuCuB-400 and AuCu-400 materials. The plot of AuCuB-400 showed a smaller diameter than that of AuCu-400 (Fig. 3A), indicating a lower interfacial charge transfer resistance. This implies that AuCuB-400 is beneficial for accelerating the electron transfer between the catalyst and reactant. The electrochemical surface areas of the AuCuB-400 and AuCu-400 materials were also tested using double-layer capacitance. AuCuB-400 presented a larger double-layer capacitance (9.84 mF cm^{-2}) than AuCu-400
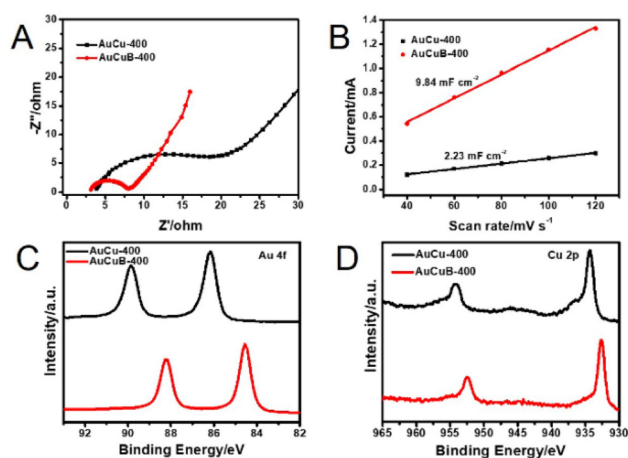

Fig. 3 Nyquist plots (A), the linear relationship between the current and scan rate (B), high-resolution XPS spectra of Au 4f (C) and Cu 2p (D) of AuCu-400 (black line) and AuCuB-400 (red line).

(2.23 mF cm^{-2}, Fig. 3B and Fig. S8†), implying a larger electrochemical active surface area which is beneficial for promoting CO_2RR.

It is hypothesized that the high activity of the catalyst is caused by B doping, which can affect the local electronic structure.[28] Hence, this study analyzed the local electronic structure of AuCuB using X-ray photoelectron spectroscopy (XPS). As shown in Fig. 3C, Au 4f in AuCuB-400 had two distinct characteristic peaks with binding energies of 84.54 and 88.22 eV for Au 4f$_{7/2}$ and Au 4f$_{5/2}$, respectively.[38] The Cu 2p$_{1/2}$ and Cu 2p$_{3/2}$ peaks appeared at 932.72 and 952.52 eV for Cu 2p, corresponding to a valence of Cu(0) or Cu(I) (Fig. 3D).[39] Au 4f and Cu 2p significantly shifted to a higher binding energy in AuCuB-400 compared with AuCu-400, implying that charge transfer occurred between B and AuCu.[40,41] Fig. S9† shows the charge density difference of AuCuB with and without B doping, in which charge transfer from the metal to B is apparently shown. The charge transfer may affect the adsorption of intermediates and further influence the electrocatalytic performance.

To further explore the reaction process, operando Raman spectroscopy experiments were conducted from 0.15 to −0.45 V *vs.* RHE in CO_2-saturated 1 M KOH solution. Herein, the reference potential was 0.15 V *vs.* RHE (CO_2RR did not occur at this potential). As shown in Fig. 4, due to the adsorption of *CO on Cu and Cu–CO stretching, AuCu-400 exhibited the Raman peaks at 301 and 389 cm^{-1}, while the corresponding Raman peaks of AuCuB-400 were at 272 and 354 cm^{-1}. The charge transfer between the B atom and AuCu was mostly responsible for the blue shift after B doping.[42,43] The absence of a *CO adsorption peak on Au was possibly caused by the rather weak binding strength of *CO and its fast desorption from Au surfaces, which correlated well with the previous study by Dunwell *et al.*[44] Notably, Cu–CO and *CO on AuCuB-400 were detected at more positive potential (0.1 V *vs.* RHE) than those on AuCu-400 (−0.25 V *vs.* RHE), indicating
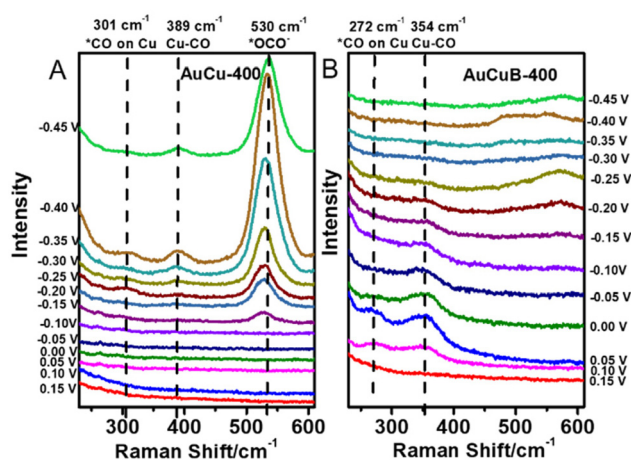
Fig. 4 Potential-dependent operando Raman spectra recorded on AuCu-400 (A) and AuCuB-400 (B) in 1 M KOH.

that the activation of CO_2 can be achieved at more positive potential and the superior activity of AuCuB converts CO_2 into CO. The LSV curves perfectly represented the results.

The *CO bridge and *CO stretching peaks appeared at 1860 and 2060 cm^{-1} (Fig. S10†) for AuCu-400, representing the key intermediate for C–C coupling.[45–50] Nevertheless, neither of these *CO peaks was observed in the Raman spectra of AuCuB-400, indicating that incorporating B is not in favor of the formation of C_2 intermediates, which coincides with the electrolysis result (Fig. 2C). As shown in Fig. 4A, the *OCO⁻ intermediate at 530 cm^{-1} was detected for AuCu-400, which is

the key intermediate for generating HCOOH.[46] In contrast, no *OCO⁻ peak was observed in the Raman spectra of AuCuB-400 (Fig. 4B), indicating that incorporating B inhibits the generation of HCOOH in CO_2 electroreduction.

DFT calculations were performed to explore the role of the incorporated B in the AuCu intermetallic compound in the conversion of CO_2 to CO [refer to the ESI for details, eqn (S6)–(S8)†].[51] A AuCu(111) facet (Fig. S11A†) was used as the model surface because of its high thermodynamic stability. The doped B was introduced as an interstitial atom at the octahedral site between the topmost layer and sublayer of AuCu (111) (Fig. S11B†), denoted as AuCu(111)-B. Such a model has been proposed in previous experimental and theoretical studies.[28,52] The CO_2 reduction to CO proceeds through two proton-coupled electron transfer (PCET) steps and *via* the formation of *COOH, followed by a C–O bond break to yield CO.[53] Adsorption configurations of *COOH and *CO on AuCu (111) and AuCu(111)-B are shown and compared in Fig. 5A. The free energy changes were obtained according to the computational hydrogen electrode model, proposed by Norskov.[54,55] Fig. 5B shows the Gibbs free energy profiles of CO_2RR to form CO. The formation of *COOH requires a high energy gain, making it the dominant process in CO_2RR to form CO and determining the limiting potential. The *COOH formation on AuCu(111)-B requires lower free energy gain (1.01 eV) than that on AuCu(111) (1.25 eV), demonstrating the easier formation of *COOH on the AuCu(111)-B surface. The solvation effect was also considered using the VASPSol code interfaced with VASP (Fig. S12†).[56] The overall trend remains identical with the one having no solvation effect. The stronger
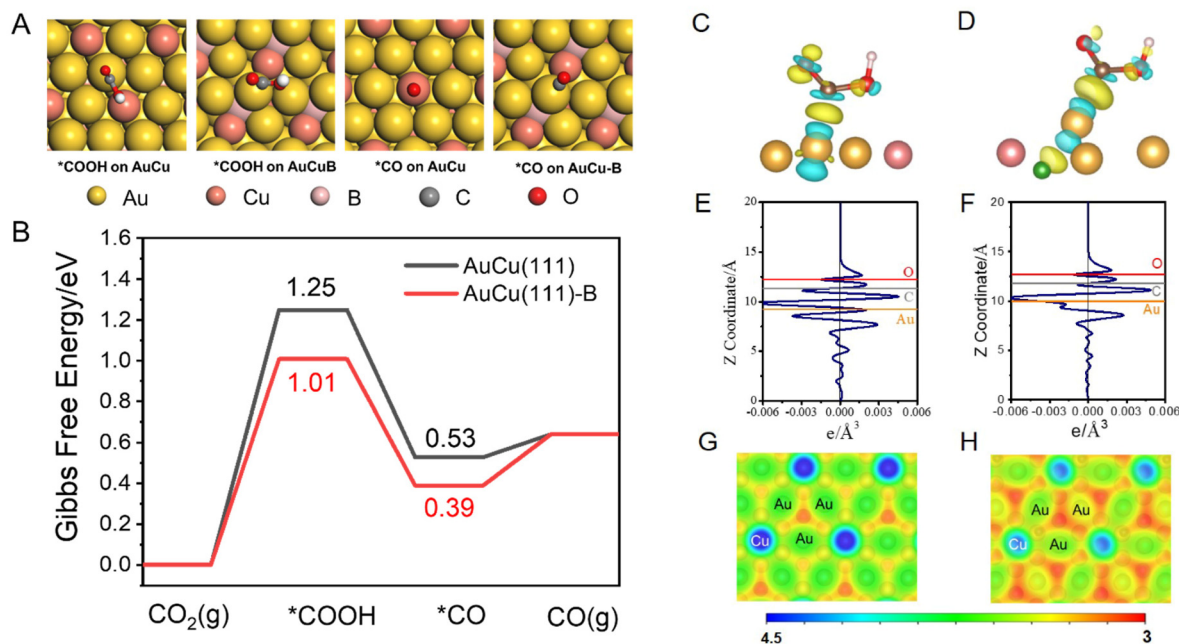

Fig. 5 (A) Adsorption configurations of *COOH and *CO on AuCu(111) and AuCu(111)-B. (B) Gibbs free energy profiles for CO_2RR on AuCu(111) and AuCu(111)-B. Charge density difference plots of *COOH adsorption on AuCu(111) (C) and AuCu(111)-B (D). Planar-averaged charge density difference of *COOH adsorption on AuCu(111) (E) and AuCu(111)-B (F). Surface electrostatic potentials of AuCu(111) (G) and AuCu(111)-B (H).

*COOH binding on AuCu(111)-B can be also observed from the charge density difference (CDD) plots (Fig. 5C and D). The *COOH radical binds to surface Au *via* the C atom on both surfaces and the Au atom donates electrons to C and O atoms in the carbonyl group. For *COOH binding on the AuCu(111)-B surface, more electron transfer is observed from the planar-averaged CDD along the Z direction. As shown in Fig. 5E and F, compared with AuCu(111), more electron depletion around Au and more electron accumulation around C and O are exhibited for the AuCu(111)-B surface. Such a phenomenon can be understood from the surface electrostatic potential (Fig. 5G and H). The regions among surface Au (shown in red) have a more negative electrostatic potential on AuCu(111)-B than on AuCu(111), indicating the higher ability for the adsorption of electrophiles (*COOH in this case). To summarize, the doping of B into the AuCu(111) surface gives rise to the higher nucleophilicity of the Au surface and thus the stronger ability for *COOH adsorption. As a consequence, the free energy gain of CO_2 that undergoes a PCET step to give *COOH is lowered on AuCu (111)-B than on AuCu(111) and the rate is accelerated by 4 orders of magnitude.

In summary, this study successfully prepared the AuCuB material using a simple one-pot method. The synthesized AuCuB-400 catalysts exhibited superior performance to the AuCu-400 alloy. The FE_{CO} of AuCuB-400 even reached 99% with a partial current density of 76 mA cm^{-2} at −1.16 V. Combining operando Raman spectroscopy with DFT calculations reveals that B doping is crucial in determining the high activity of the catalyst by tuning the electronic structures and thus the strong ability for *COOH adsorption on AuCuB. These findings will serve as a good strategy for the high performance of CO_2 electroreduction to form CO.

Author contributions

H. W. and J. L. conceived the idea for the project. Y. L. performed the design of electrocatalytic experiments and the structural characterization. Y. L. and H. W. conducted the performance measurements and data analysis. Y. F. and Q. Y. performed the DFT calculations. Y. L. and Y. F. wrote the manuscript. H. W., J. L. and Q. Y. supervised the project. All authors discussed the results and commented on the manuscript at all stages.

Conflicts of interest

The authors declare no conflicts of interest.

Acknowledgements

References

1 F. Orsini and P. Marrone, *J. Cleaner Prod.*, 2019, **241**, 118380.
2 M. Aresta, A. Dibenedetto and A. Angelini, *Chem. Rev.*, 2014, **114**, 1709–1742.
3 S. Overa, T. G. Feric, A.-H. A. Park and F. Jiao, *Joule*, 2021, **5**, 8–13.
4 J. B. Greenblatt, D. J. Miller, J. W. Ager, F. A. Houle and I. D. Sharp, *Joule*, 2018, **2**, 381–420.
5 D. G. Nocera, *Acc. Chem. Res.*, 2017, **50**, 616–619.
6 P. De Luma, C. Hahn, D. Higgins, S. A. Jaffer, T. F. Jaramillo and E. H. Sargent, *Science*, 2019, **364**, eaav3506.
7 J. Liang, D. Chen, X. Yao, K. Zhang, F. Qu, L. Qin, Y. Huang and J. Li, *Small*, 2020, **16**, 1903398.
8 S. Overa, B. H. Ko, Y. Zhao and F. Jiao, *Acc. Chem. Res.*, 2022, **55**, 638–648.
9 Y. Cheng, P. Hou, X. Wang and P. Kang, *Acc. Chem. Res.*, 2022, **55**, 231–240.
10 I. Siewert, *Acc. Chem. Res.*, 2022, **55**, 473–483.
11 L. Li, X. Li, Y. Sun and Y. Xie, *Chem. Soc. Rev.*, 2022, **51**, 1234–1252.
12 G. Wang, J. Chen, Y. Ding, P. Cai, L. Yi, Y. Li, C. Tu, Y. Hou, Z. Wen and L. Dai, *Chem. Soc. Rev.*, 2021, **50**, 4993–5061.
13 K. P. Kuhl, E. R. Cave, D. N. Abram and T. F. Jaramillo, *Energy Environ. Sci.*, 2012, **5**, 7050–7059.
14 X. Duan, J. Xu, Z. Wei, J. Ma, S. Guo, S. Wang, H. Liu and S. Dou, *Adv. Mater.*, 2017, **29**, 1701784.
15 T. Asefa, *Acc. Chem. Res.*, 2016, **49**, 1873–1883.
16 M. Zhou, H.-L. Wang and S. Guo, *Chem. Soc. Rev.*, 2016, **45**, 1273–1307.
17 H. Chen, Z. Li, Z. Zhang, K. Jie, J. Li, H. Li, S. Mao, D. Wang, X. Lu and J. Fu, *Ind. Eng. Chem. Res.*, 2019, **58**, 15425–15431.
18 Y. Han, Z. Wang, X. Han, W. Fang, Y. Zhou, K. Lei, B. You, H. S. Park and B. Y. Xia, *ACS Sustainable Chem. Eng.*, 2021, **9**, 2609–2615.
19 D. Siltamaki, S. Chen, F. Rahmati, J. Lipkowski and A-C. Chen, *J. Electrochem.*, 2021, **27**, 278–290.
20 D. Kim, C. Xie, N. Becknell, Y. Yu, M. Karamad, K. Chan, E. J. Crumlin, J. K. Nørskov and P. Yang, *J. Am. Chem. Soc.*, 2017, **139**, 8329–8336.
21 Z.-Q. Liang, T.-T. Zhuang, A. Seifitokaldani, J. Li, C.-W. Huang, C.-S. Tan, Y. Li, P. De Luna, C. T. Dinh, Y. Hu, Q. Xiao, P.-L. Hsieh, Y. Wang, F. Li, R. Quintero-Bermudez, Y. Zhou, P. Chen, Y. Pang, S.-C. Lo, L.-J. Chen, H. Tan, Z. Xu, S. Zhao, D. Sinton and E. H. Sargent, *Nat. Commun.*, 2018, **9**, 3828.
22 J. Xu and M. Saeys, *J. Catal.*, 2006, **242**, 217–226.
23 J. Xu and M. Saeys, *J. Phys. Chem. C*, 2009, **113**, 4099–4106.

24 J. Xu, L. Chen, K. F. Tan, A. Borgna and M. Saeys, *J. Catal.*, 2009, **261**, 158–165.

25 K. F. Tan, J. Chang, A. Borgna and M. Saeys, *J. Catal.*, 2011, **280**, 50–59.

26 K. Jiang, K. Xu, S. Zou and W.-B. Cai, *J. Am. Chem. Soc.*, 2014, **136**, 4861–4864.

27 C. W. A. Chan, A. H. Mahadi, M. M.-J. Li, E. C. Corbos, C. Tang, G. Jones, W. C. H. Kuo, J. Cookson, C. M. Brown, P. T. Bishop and S. C. E. Tsang, *Nat. Commun.*, 2014, **5**, 5787.

28 Y. Zhou, F. Che, M. Liu, C. Zou, Z. Liang, P. De Luna, H. Yuan, J. Li, Z. Wang, H. Xie, H. Li, P. Chen, E. Bladt, R. Quintero-Bermudez, T.-K. Sham, S. Bals, J. Hofkens, D. Sinton, G. Chen and E. H. Sargent, *Nat. Chem.*, 2018, **10**, 974–980.

29 T.-T. Zhuang, Z.-Q. Liang, A. Seifitokaldani, Y. Li, P. De Luna, T. Burdyny, F. Che, F. Meng, Y. Min, R. Quintero-Bermudez, C. T. Dinh, Y. Pang, M. Zhong, B. Zhang, J. Li, P.-N. Chen, X.-L. Zheng, H. Liang, W.-N. Ge, B.-J. Ye, D. Sinton, S.-H. Yu and E. H. Sargent, *Nat. Catal.*, 2018, **1**, 421–428.

30 J.-Y. Wang, Y.-Y. Kang, H. Yang and W.-B. Cai, *J. Phys. Chem. C*, 2009, **113**, 8366–8372.

31 Y. Okamoto, Y. Nitta, T. Imanaka and S. Teranishi, *J. Chem. Soc., Faraday Trans.*, 1979, **75**, 2027–2039.

32 B. Hammer and J. K. Norskov, *Nature*, 1995, **376**, 238–240.

33 Y. Li, H. Yu, Z. Wang, S. Liu, Y. Xu, X. Li, L. Wang and H. Wang, *Chem. Commun.*, 2019, **55**, 14745–14748.

34 J. Li, J. Chen, Q. Wang, W.-B. Cai and S. Chen, *Chem. Mater.*, 2017, **29**, 10060–10067.

35 Y. Xu, S. Yu, T. Ren, C. Li, S. Yin, Z. Wang, X. Li, L. Wang and H. Wang, *J. Mater. Chem. A*, 2020, **8**, 2424–2429.

36 B. Jiang, X.-G. Zhang, K. Jiang, D.-Y. Wu and W.-B. Cai, *J. Am. Chem. Soc.*, 2018, **140**, 2880–2889.

37 C. Chen, X. Sun, L. Lu, D. Yang, J. Ma, Q. Zhu, Q. Qian and B. Han, *Green Chem.*, 2018, **20**, 4579–4583.

38 Q. Liu, Q. Chen, T. Li, Q. Ren, S. Zhong, Y. Zhao and S. Bai, *J. Mater. Chem. A*, 2019, **7**, 27007–27015.

39 H. Li, T. Liu, P. Wei, L. Lin, D. Gao, G. Wang and X. Bao, *Angew. Chem., Int. Ed.*, 2021, **60**, 14329–14333.

40 Y. Mi, S. Shen, X. Peng, H. Bao, X. Liu and J. Luo, *ChemElectroChem*, 2019, **6**, 2393–2397.

41 H. Li, T.-W. Jiang, X. Qin, J. Chen, X.-Y. Ma, K. Jiang, X.-G. Zhang and W.-B. Cai, *ACS Catal.*, 2021, **11**, 6846–6856.

42 X. Yan, C. Chen, Y. Wu, S. Liu, Y. Chen, R. Feng, J. Zhang and B. Han, *Chem. Sci.*, 2021, **12**, 6638–6645.

43 K. K. Patra, S. Park, H. Song, B. Kim, W. Kim and J. Oh, *ACS Appl. Energy Mater.*, 2020, **3**, 11343–11349.

44 M. Dunwell, Q. Lu, J. M. Heyes, J. Rosen, J. G. Chen, Y. Yan, F. Jiao and B. Xu, *J. Am. Chem. Soc.*, 2017, **139**, 3774–3783.

45 A. Herzog, A. Bergmann, H. S. Jeon, J. Timoshenko, S. Kühl, C. Rettenmaier, M. Lopez Luna, F. T. Haase and B. Roldan Cuenya, *Angew. Chem., Int. Ed.*, 2021, **60**, 7426–7435.

46 W. Shan, R. Liu, H. Zhao, Z. He, Y. Lai, S. Li, G. He and J. Liu, *ACS Nano*, 2020, **14**, 11363–11372.

47 D. Ren, B. S.-H. Ang and B. S. Yeo, *ACS Catal.*, 2016, **6**, 8239–8247.

48 Y. Deng and B. S. Yeo, *ACS Catal.*, 2017, **7**, 7873–7889.

49 Q. Wang, K. Liu, J. Fu, C. Cai, H. Li, Y. Long, S. Chen, B. Liu, H. Li, W. Li, X. Qiu, N. Zhang, J. Hu, H. Pan and M. Liu, *Angew. Chem., Int. Ed.*, 2021, **60**, 25241–25245.

50 H. An, L. Wu, L. D. B. Mandemaker, S. Yang, J. de Ruiter, J. H. J. Wijten, J. C. L. Janssens, T. Hartman, W. van der Stam and B. M. Weckhuysen, *Angew. Chem., Int. Ed.*, 2021, **60**, 16576–16584.

51 X. Kong, Y. Liu, P. Li, J. Ke, Z. Liu, F. Ahmad, W. Yan, Z. Li, Z. Geng and J. Zeng, *Appl. Catal., B*, 2020, **268**, 118452.

52 Z. Wang, J. Niu, Y. Xu, L. Wang, H. Wang and H. Liu, *ACS Sustainable Chem. Eng.*, 2020, **8**, 12588–12594.

53 Y. Li, S. H. Chan and Q. Sun, *Nanoscale*, 2015, **7**, 8663–8683.

54 J. K. Nørskov, J. Rossmeisl, A. Logadottir, L. Lindqvist, J. R. Kitchin, T. Bligaard and H. Jónsson, *J. Phys. Chem. B*, 2004, **108**, 17886–17892.

55 J. K. Nørskov, T. Bligaard, A. Logadottir, J. R. Kitchin, J. G. Chen, S. Pandelov and U. Stimming, *J. Electrochem. Soc.*, 2005, **152**, J23.

56 K. Mathew, R. Sundararaman, K. Letchworth-Weaver, T. A. Arias and R. G. Hennig, *J. Chem. Phys.*, 2014, **140**, 084106.